SPECTRAL VARIATIONS AND A CLASSICAL CURVE-OF-GROWTH ANALYSIS OF HDE 226868 (CYG X-1)

G. Canalizo[1], G. Koenigsberger, D. Peña, and E. Ruiz

Instituto de Astronomía
Universidad Nacional Autónoma de México

RESUMEN

Se presenta el análisis de espectros de alta dispersión en el rango espectral 3200–6800 A del sistema binario HDE 226868, la contraparte óptica de Cyg X-1, obtenidos en el Observatorio Astronómico Nacional en San Pedro Mártir. Se obtienen las correlaciones de velocidad radial vs. potencial de excitación de las líneas para 7 de las fases orbitales; se encuentra que la pendiente de esta correlación es mayor en fases orbitales cercanas a 0.5 (cuando el objeto colapsado se encuentra "enfrente" de la compañera) lo que coincide con la predicción de Friend & Castor (1982) basada en la distorsión de la superficie de la supergigante introducida por el campo gravitacional del agujero negro. Se detectan variaciones en los perfiles de las líneas en absorción que sugieren contaminación de éstas por componentes en emisión. Se efectúa un análisis clásico (i.e., LTE) de curva de crecimiento del cual se obtiene una temperatura de excitación $T_{exc} = 32100 \pm 1600$ °K y una sobreabundancia de He con respecto a la supergigante B0Ia ϵ Ori.

ABSTRACT

We present an analysis of high resolution (R ∼ 17000) echelle spectra in the wavelength range 3200 to 6800 A obtained at the Observatorio Astronómico Nacional at San Pedro Mártir[2], of HDE 226868, the optical component of the Cyg X-1 binary system. Empirical radial velocity vs. excitation (RV vs. E) relations are obtained from the spectra at 7 orbital phases and the slope *(A)* of these relations is found to vary, having two extrema: -0.30 km s^{-1} eV^{-1} near phase 0.5 (collapsed object "in front") and -0.22 km s^{-1} eV^{-1} near phase 0.0. At other phases the value is $A = -0.13$ km s^{-1} eV^{-1}. This variability in the slope of the RV vs. E relation is in very good agreement with the theoretically predicted anisotropic mass-loss rates resulting from the modified gravitational potential of the system (Friend & Castor 1982) for the case in which the primary star fills its Roche lobe. Variations at the 25% level in the shapes and strengths of Hβ and He I photospheric absorption lines are detected. The variability of the absorption line profiles appears to correlate with the Hα and the He II 4686 A emission line variations, suggesting that the absorption lines are contaminated by variable emission components. From a classical curve-of-growth analysis HDE 226868 is found to have $T_{exc} = 32100 \pm 1600$ °K, and to be overabundant in He and underabundant in C with respect to the B0Ia supergiant ϵ Ori.

[1] Current address: Institute for Astronomy, University of Hawaii.

[2] The Observatorio Astronómico Nacional at San Pedro Mártir (OAN/SPM) of the the Instituto de Astronomía of the Universidad Nacional Autónóma de México.

1. INTRODUCTION

The existence of binary systems containing collapsed companions is predicted by the models which have been developed to describe the evolution of mas-

sive stars (van de Heuvel 1976; and see Chiosi & Maeder 1986 for a review). Different systems containing collapsed companions may display different spectroscopic characteristics, depending on the initial conditions (mass and initial chemical element abundances of the components, their orbital separation and the angular momentum of the system) and on the evolutionary stage. In most of the cases in which the massive, optically visible component of the system is an OB star, the unseen companion is a neutron star. In a few cases such as in Cyg X-1, A0620–00, and LMC X-3 there is strong evidence pointing to the presence of a black hole. The evidence for a black hole lies basically in the determination of the mass of the OB components.

In order to understand the physical processes which occur in binary X-ray systems, it is necessary to have a precise knowledge of the properties of the optically visible star, including its mass-loss characteristics. In recent years, very powerful tools for the analysis of stellar spectra have been developed. In particular, non-LTE multilevel radiation transfer codes have been constructed which allow the determination of basic stellar parameters with precisions never before attainable (see review by Kudritzki & Hummer 1990). By the fitting of synthetic line profiles produced with the stellar atmospheres codes to the observed line profiles it is possible to determine T_{eff}, log g and chemical abundances. For this, it is necessary to obtain high resolution, large signal-to-noise ratio spectra with a good wavelength coverage to allow the use of lines of different elements and a wide range in ionization and excitation potentials.

There are, however, important uncertainties in the results derived from the application of these methods to stars in close binary systems due to the fact that interaction effects between the two stars in the system can lead to distortions in the spectral characteristics. The interaction effects in massive X-ray binary systems that may lead to distortions in the normal star's photospheric absorption line profiles include: the altered gravitational potential, the heating of the normal star's atmosphere by the X-rays emitted by the collapsed companion, and the presence of an accretion disc and/or shock front associated with the collapsed object. These effects are expected to introduce orbital phase-dependent variations which can be used to identify them. It is thus of interest to search for such variations and to use them to quantify the magnitude of the interaction effects on the spectrum. This can allow constraints to be placed on the reliability with which intrinsic characteristics of the normal star can be derived from fitting non-LTE models to the line profiles.

Friend & Castor (1982) analyzed the properties of a radiation-driven stellar wind in X-ray binary systems and found that there is enhanced mass-loss along the line joining the two stars. In the specific case of HDE 226868 (Cyg X-1), they found the mass-loss rate to be very non-spherically symmetric, deriving an angular mass flux at orbital phase 0.5 (the O-star's surface facing the collapsed companion) that was a factor of 3 to 4 larger than at other orbital phases. In their calculation the X-ray heating effects were neglected, the principal effect causing this asymmetry being the modified gravitational potential due to the presence of the companion. Clearly, the modified gravitational potential should also affect the properties of the photosphere of the supergiant, not just its wind, and thus, it is of interest to search for this effect in the spectrum. One diagnostic of such an effect is the radial velocity vs. excitation (RV vs. E) correlation.

The RV vs. E correlation was first discoverd by Hutchings (1968a, 1968b) in Of stars. In these stars, the radial velocities of photospheric lines arising from atomic transitions from levels of lower excitation are more negative with respect to the systemic velocity than lines of higher excitation transitions. This effect is attributed to the presence of a velocity gradient and an excitation gradient in the stellar atmosphere. The observed gradient in the radial velocities of the photospheric lines indicates that most of these spectral features are formed in the region near the star where a stellar wind is developing and the atmosphere is starting to accelerate outward. In these regions, the excitation temperature falls with increasing radius, so that the acceleration can be observed as an increase of outward velocity with falling ionization and excitation. Hence, if temperature decreases with radius and velocity increases monotonically with radius, the slope of the correlation should be indicative of the combined rate of change. Hutchings (1976a) was the first to suggest that the slope might be expected to correlate with mass loss rate in the sense that steeper slopes imply larger mass loss rates. Thus, if the modified gravitational potential plays a significant role in determining the mass-loss characteristics, then a variation in the value of the slope of the RV vs. E correlation as a function of orbital phase should be present. Indeed, there is some indication that in binaries, such as 29 CMa, (Hutchings 1978) a variation in the slope of the RV vs. E relation is present.

In this paper we present the data for one of the best-studied black hole candidate systems, HDE 226868 (Cyg X-1). These data will serve as a basis for a more detailed analysis of interaction effects in forthcoming investigations. Here we will present the results of echelle observations that cover the wavelength range 3200–6800 Å, obtained at different orbital phases, and which permit us to address the questions of orbital phase dependent line profile variations, the RV vs. E correlation as a function of orbital phase, and a preliminary analysis of the

chemical element abundances through the classical curve-of-growth method.

HDE 226868 is a supergiant which has been classified as a normal O9.7Iab star (Walborn 1973). Its optical spectrum displays variable He II 4686 A and Hα emission lines. The intense X-ray luminosity of the system ($L_X \sim 10^{38}$ ergs s^{-1}) indicates the presence of a collapsed object. The binary orbital period is 5.6 days, as derived from the radial velocity variations in the photospheric lines in the spectrum. The mass function of this system indicates that, if the optically visible star has a mass typical of O9.7Iab supergiants, then the collapsed companion has a mass of 10–13 $M_\odot$, much in excess of what is allowed for neutron stars, and hence it must be a black hole. This conclusion can be avoided if it is assumed that the system is triple, and that the unseen companion is really two stars. Shafter et al. (1980) analyzed the possibility, but there has been little evidence supporting this hypothesis.

Oda (1977) reviewed the X-ray characteristics derived from the early X-ray observations. There are no variations in the X-ray flux indicative of eclipses in the 5.6-day orbital period, but Priedhorsky, Terrell, & Holt (1983) have found that the X-ray flux varies by 25% with a 294 day period. Kemp et al. (1983) have found variations on the 1% level in the optical light with similar timescales, but this longer timescale variability is not found in the radial velocity measurements of the supergiant.

Treves et al. (1980) reported the results of ultraviolet, X-ray and infrared observations of HDE 226868 and find that the general shape of the spectrum is that expected from a late O supergiant. Gies & Bolton (1986a) undertook a detailed study of the optical line spectrum, and found no evidence for significant variations of the spectral type about the mean value of O9.7Iab, as a function of orbital phase. In addition, they found all the absorption line strengths to be normal for this spectral type. This indicates that the contribution from any possible additional continuum sources within the system must be very small. Furthermore, Ninkov, Walker, & Yang (1987) studied the absorption line spectrum, comparing it to the spectrum of a single star of similar spectral type and they, too, found that there is no significant difference in strength of metal lines between the spectrum of HDE 226868 and that of other stars of the same spectral type. Thus, the observational evidence obtained thus far indicates that, with the exception of the variable emission lines at He II 4686 A and at Hα, the spectrum of the optically visible star is normal for its spectral type.

There are a number of orbital phase related variations which occur in the spectra of HDE 226868. Treves et al. (1980) report changes in the equivalent widths of UV absorption lines. Particularly striking is the variation in the Si IV doublet which can be

observed in their Figure 3, where these absorption lines vanish at phase 0.54 (when the collapsed object is "in front") while at phases close to 0.0 they are quite prominent. Davis & Hartmann (1983) used the UV P Cygni profiles to estimate the terminal velocity in the supergiant's wind, and found it to be dependent on the orbital phase: at phase 0.5 the measured terminal speed is ~ 1500 km s^{-1} while in the undisturbed wind (at opposite orbital phases phases) it is 2300 km s^{-1}. The lower wind speed in the direction of the collapsed companion as well as the disappearance of the Si IV P Cyg absorptions is most likely the result of X-ray heating of the stellar wind by the intense X-ray source, and is known as the "Hatchett – McCray" effect (Hatchett & McCray 1977). Aab (1983b) and Ninkov et al. (1987) analyzed the He II 4686 A emission feature in an effort to separate the emission line from the underlying photospheric absorption line. The result of both investigations yields a He II 4686 A emission-line radial velocity curve that has a phase lag with respect to the radial velocity curve one would expect if the He II line were associated only with the secondary component. These results all indicate that interaction effects are present at least at the level of the stellar wind.

The structure of this paper is as follows: In § 2 we describe the observations and data reduction; in § 3 the results and a discussion are presented of the equivalent widths, the RV vs. E relation, the curve of growth-derived abundances, and the line profile variability; in § 4 we summarize the conclusions.

2. OBSERVATIONS AND DATA REDUCTION

The observations were carried out on 1991 August 17–21, 1993 June 25–30, 1993 October 8–13, and 1994 June 1–5 with the 2.1-m telescope of the Observatorio Astronómico Nacional at San Pedro Mártir (OAN/SPM) using the REOSC echelle system. Two camera systems were used. Spectra of 1993 October and 1994 were acquired with the recently installed UCL camera (Echevarría & Diego 1995) which allows direct use of a CCD detector system. Pixel size of the 1024 × 1024 Thompson THX31156 CCD detector used for these observations is 19 × 19 μm. The chip comes with a Metachrome II coating to improve blue response. Its quantum efficiency at 7000 A is about 40% and at 4000 A about 15%. Further specifications may be found in Peña & Torres-Peimbert (1992) and are summarized by Levine & Chakrabarty (1994). With the 300 lines mm^{-1} echellete, the system gives a resolution of 7.8 A mm^{-1} (0.15 A pixel^{-1}) at Hβ and 10.7 A mm^{-1} (0.20 A pixel^{-1}) at Hα. The resolution is R = 17000, which corresponds to 17 km s^{-1} per 2 pixels. The grating angle was set at 353° 30′, for the majority of observations, which allows simultaneous coverage of the spectral range from Hγ to

Hα. One set of spectra was obtained at an angle of 352° 26′ in order to cover the blue spectral region.

The data of 1993 July were acquired with the original REOSC camera system which was designed for use with photographic plates or a photon counting device, and to which a fiber-optics coupled CCD was adapted (Cruz-González & Carrasco 1990). This CCD is a 516 × 516 Ford Aerospace PM 512 chip with 20 × 20 μm pixel size. The fiber optics bundle is cemented to the face of the chip. Each fiber has a diameter of about 6 μm. This echelle configuration is described by Levine & Chakrabarty (1994). The slit was set at a width of 150 or 300 μm, depending on the dome "seeing". A slit width of 150 μm corresponds to a projection on the sky of 2 arcsec. On each night, a sequence of bias frames were obtained at the beginning and at the end of the night,

as well as sequences of flat fields, using an incandescent lamp. Cyg X-1 was observed in general with 15 min exposure times, in a sequence of 3 or more exposures, preceded and followed by an exposure of a Th-Ar comparison lamp. In Table 1 we present the journal of our observations.

Data reduction was performed with IRAF, using the standard reduction procedures. Wavelength calibrations were made using the least-mean-squares fit to identified lines in the Th-Ar spectrum (Peña, Canalizo, & Koenigsberger 1994), after bias correction. The instrumental response of each order was removed by fitting a polynomial (usually of third or fourth order) to the data of each spectral order, for each spectrum, and dividing the data by this polynomial. In most the spectral orders, the procedure produced a flat normalized spectrum. This is not the

TABLE 1

JOURNAL OF OBSERVATIONS[a]

HJD 2449000.+	Exposure Time (s)	Range (A)	Orbital Phase	HJD 2449000.+	Exposure Time (s)	Range (A)	Orbital Phase
164.76	1800	5800–6600	0.880	536.79	900	4340–6800	0.319
164.94	1800	5800–6600	0.911	536.80	900	4340–6800	0.321
165.73	1800	5800–6600	0.053				
166.71	1800	5800–6600	0.228	536.82	900	4340–6800	0.325
166.74	1800	5800–6600	0.232	536.84	900	4340–6800	0.327
166.76	1800	5800–6600	0.237	536.86	900	4340–6800	0.330
270.63	900	4200–6650	0.786	536.88	900	4340–6800	0.335
270.64	900	4200–6650	0.789	536.89	900	4340–6800	0.337
271.63	900	4200–6650	0.965	536.91	900	4340–6800	0.339
271.74	900	4200–6650	0.985	536.92	900	4340–6800	0.342
				536.93	900	4340–6800	0.344
271.76	900	4200–6650	0.987	537.79	900	3200–5525	0.497
271.78	900	4200–6650	0.992	537.80	900	3200–5525	0.499
273.67	900	4200–6650	0.330				
273.69	900	4200–6650	0.332	537.82	900	3200–5525	0.502
273.70	900	4200–6650	0.335	537.84	900	4340–6800	0.506
273.72	900	4200–6650	0.338	537.86	900	4340–6800	0.509
273.73	900	4200–6650	0.340	537.87	900	4340–6800	0.511
427.99	900	3940–6475	0.889	537.88	900	4340–6800	0.513
535.73	900	4340–6800	0.129	537.89	900	4340–6800	0.516
535.74	900	4340–6800	0.131	537.91	900	4340–6800	0.518
535.83	900	4340–6800	0.147	537.97	900	4340–6800	0.529
535.94	900	4340–6800	0.167	538.77	900	4350–6800	0.672
535.96	900	4340–6800	0.170	538.78	900	4350–6800	0.674
536.72	900	4340–6800	0.305				
536.73	900	4340–6800	0.308	538.79	900	4350–6800	0.676
536.74	900	4340–6800	0.310	538.80	900	4350–6800	0.678
536.77	900	4340–6800	0.314	538.82	900	4350–6800	0.680
536.78	900	4340–6800	0.316	538.83	900	4350–6800	0.682

[a] Observations for 1800, 5800–6600 were done with CGAIN = 0; for 900, 4200–6650 with CGAIN = 15 and the rest with CGAIN = 60.

case for order 34 (containing Hα), where a satisfactory fit to the entire order was not achieved, and the fit was made to the central portions of the order only.

In Figure 1 we present the spectrum of HDE 226868 at orbital phase 0.51 (collapsed companion "in front") for the wavelength range 3200–6800 A. This spectrum is the average of 3 spectra in the region 3200–4400 A, and 7 spectra in the region 4400–6800 A. In Table 2 we list the S/N ratios for the average spectrum illustrated in Figure 1, which range from ∼ 10 at 3300 A to ∼ 225 at 6500 A. This table can be used to assess the significance of the features present in Figure 1.

TABLE 2

SIGNAL TO NOISE RATIOS FOR FIGURE 1

Wavelength Range	S/N	Wavelength Range	S/N	Wavelength Range	S/N
3200–3350	9	4400–4550	78	5600–5750	171
3350–3500	17	4550–4700	81	5750–5900	184
3500–3650	23	4700–4850	85	5900–6050	173
3650–3800	37	4850–5000	96	6050–6200	216
3800–3950	46	5000–5150	129	6200–6350	195
3950–4100	50	5150–5300	150	6350–6500	225
4100–4250	52	5300–5450	157	6500–6650	213
4250–4400	70	5450–5600	158	6650–6800	215

The equivalent widths were measured on each individual spectrum with IRAF by visually interpolating the continuum level, and integrating in wavelength over the width of the line. Most of the lines are relatively symmetric, and the position where the line meets the continuum level can be determined directly. However, some lines (for example, He lines) present asymmetries in their wings. In these cases, the width given by the less extended wing was preferred, and thus these measurements represent a lower limit to the value of the equivalent width. Radial velocities were measured by finding the midpoint of the profiles at the half intensity level. Velocities were corrected for the Earth+Sun motion. The orbital radial velocity curve of Gies & Bolton (1986a,b) was used to convert the radial velocities to the frame of reference of the primary star.

3. RESULTS AND DISCUSSION

3.1. Line Identifications and Equivalent Width Variations

In Table 3 we present the list of absorption lines which are present in each individual spectrum and

their equivalent widths. The identifications are based on the line list of Striganov & Svetitskii (1968), Lamers (1972b), Gies & Bolton (1986), Traving (1957) and Herbig (1995). In columns 1 and 2 we list the laboratory wavelength and ionic species responsible for the line; in column 3 the average of the equivalent widths measured on all spectra excluding orbital phase 0.149 (see below); and in column 4 the corresponding standard deviation, except for the wavelength range 3300–4000 A where only one set of spectra was obtained. In column 5 we list relevant comments; an asterisk indicates lines which were used for the curve of growth analysis.

In addition to the rich photospheric line spectrum and the usual ISM absorption lines, we have identified a very large number of diffuse interstellar bands (DIB's) some of which have equivalent widths as large as 170 mA. These features are of interest due to their association with regions of high ISM extinction (Herbig 1995) and thus the equivalent widths we present here will be useful for future studies of the ISM along the line of sight to HDE 226868.

In Figure 2 the mean value for each night of the measured equivalent widths (only data of 1993 October and 1994) of He I 4387, 4471, 4713, 5015, 5876 A, He II 4199, 4541 A, Si III 4552 A, and Hβ are plotted as a function of orbital phase, and compared with values published by Gies & Bolton (1986a). Our equivalent widths (triangles) of He I and Si III are, in general, very similar to those of Gies & Bolton (1986a) (circles). In the case of He II, our values are systematically smaller, which can be attributed to the fact that we measured the equivalent width over a smaller wavelength interval than did Gies & Bolton (1986a). In general, small variations in equivalent width are present in most of the lines measured, as can be seen on Figure 2. Significant variations (> 20%) are found in the equivalent width of the following lines: He I 5876, 5015 A and Hβ. Both He I lines tend to have larger equivalent widths around phase 0 than at other phases. This trend is also present in Si III 4553 A, but with a smaller amplitude.

There is one orbital phase (0.149) at which a very discrepant value of equivalent width is obtained. This is most obvious in the lines of He I 4471, 5876, 5015 and Hβ which show a significant increase in equivalent width at this phase, with respect to other phases and with respect to data of Gies & Bolton (1986a) at a nearby phase. In contrast, He II 4541 is weaker relative to other phases. The spectrum at phase 0.149 was obtained in 1994, and the variation may not be orbital phase related. The line profiles of the He I lines at phase 0.149 are peculiar with respect to other phases (see below), but further data at these orbital positions is necessary before any conclusions may be drawn as to the origin of the enhanced strength at this phase.
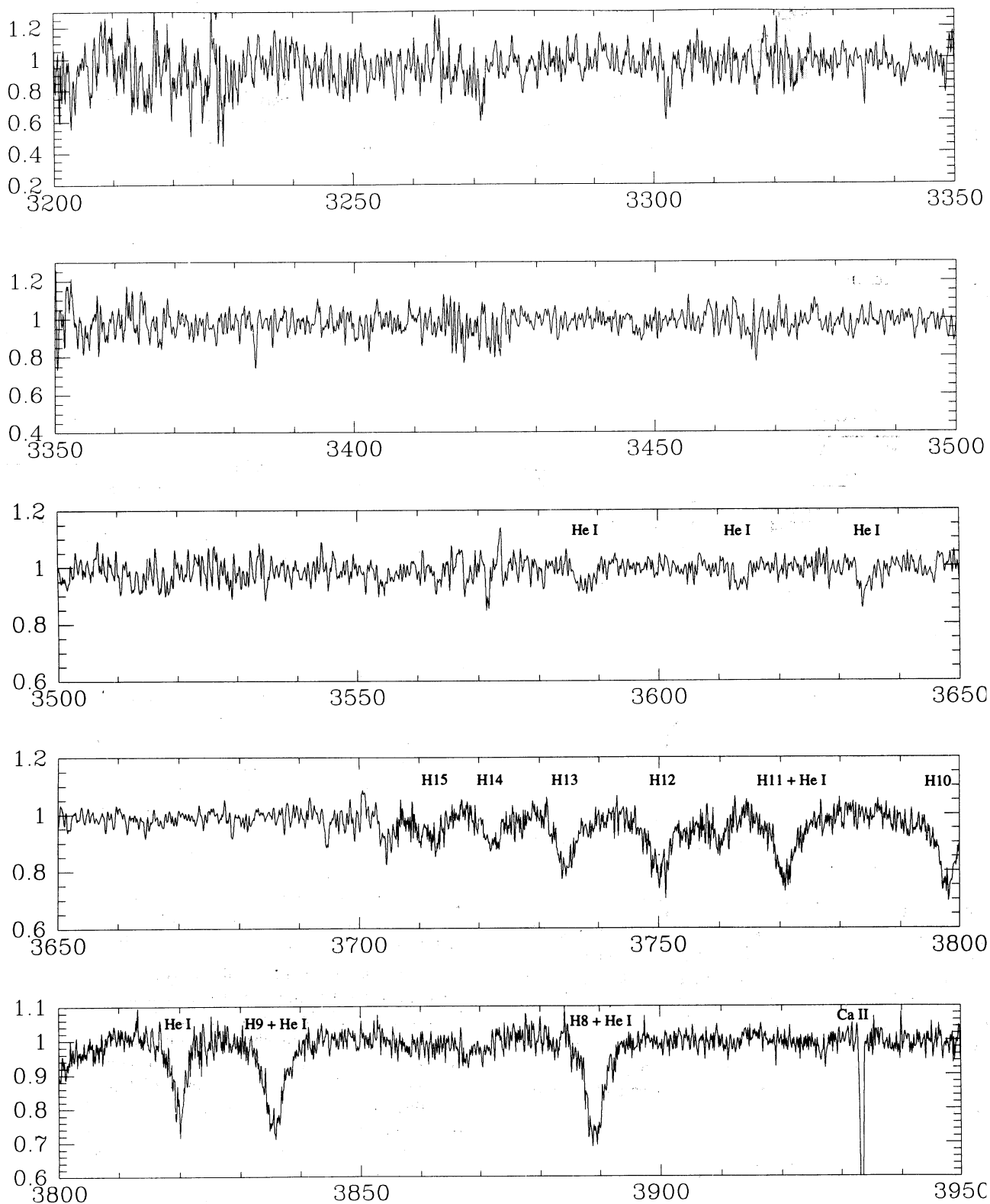
Fig. 1. Normalized spectrum of the HD 286868 binary system at orbital phase 0.51 (unseen companion "in front"). The ordinate is in units of normalized flux and the abscissa is in wavelength.
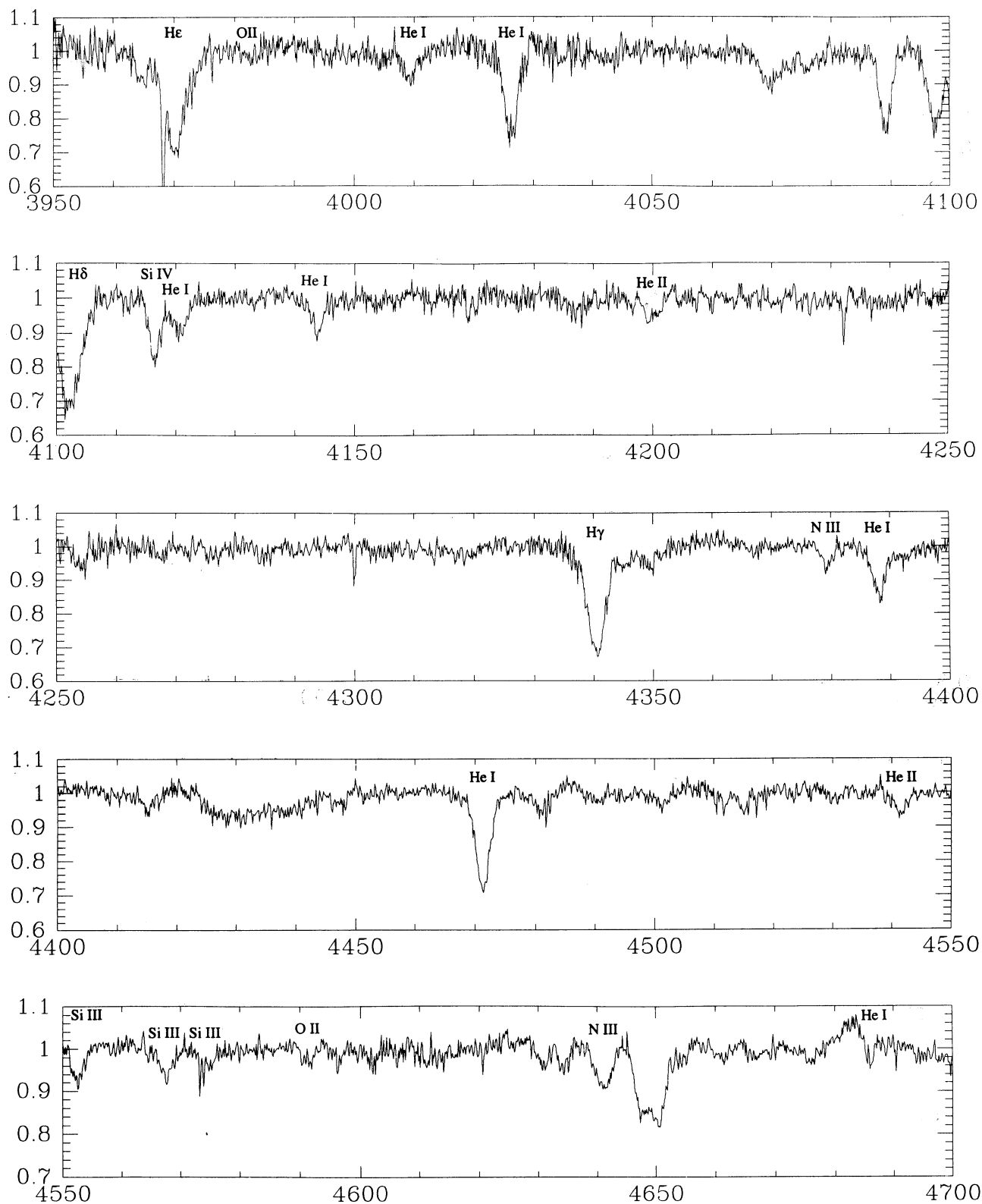
Fig. 1. Continued

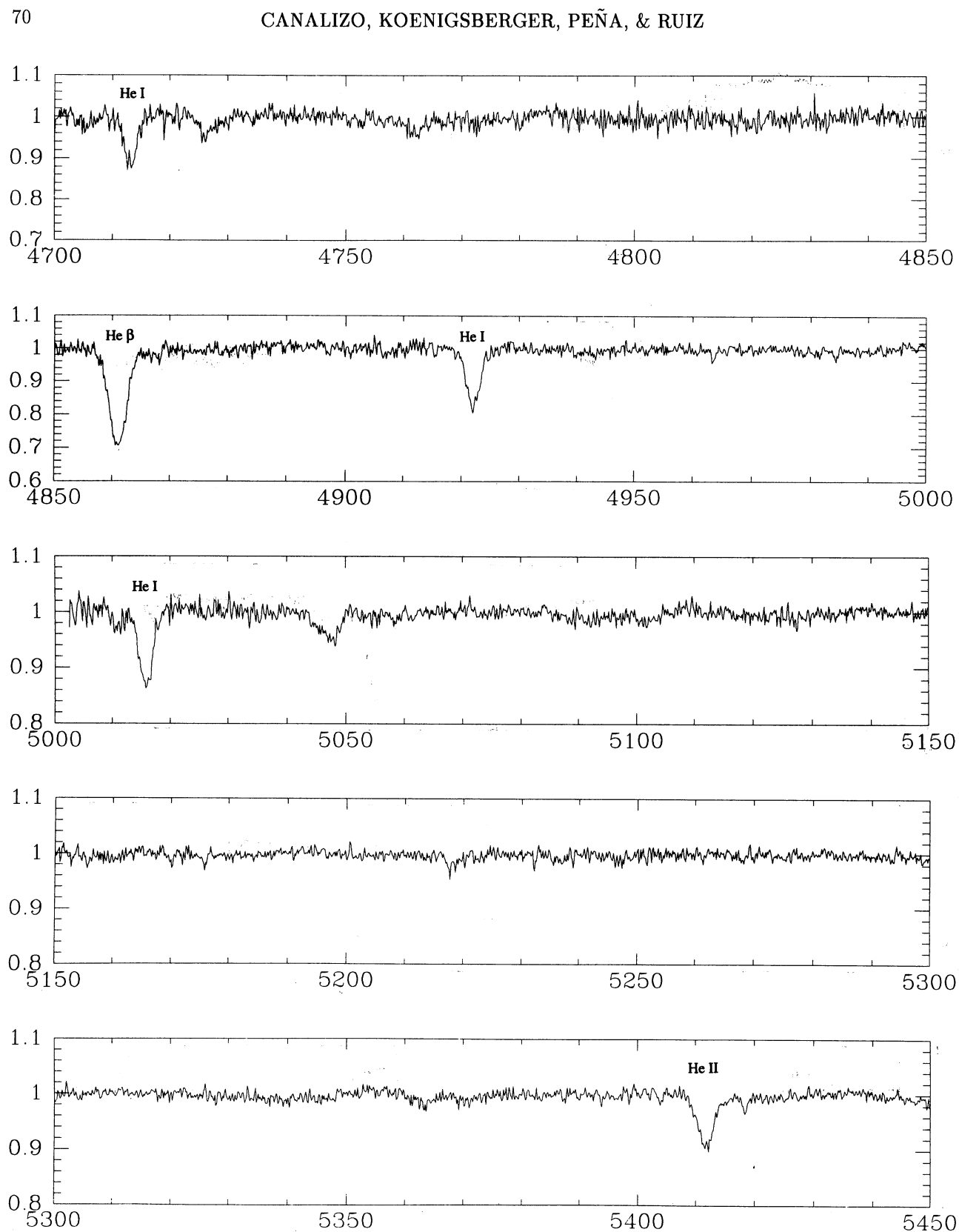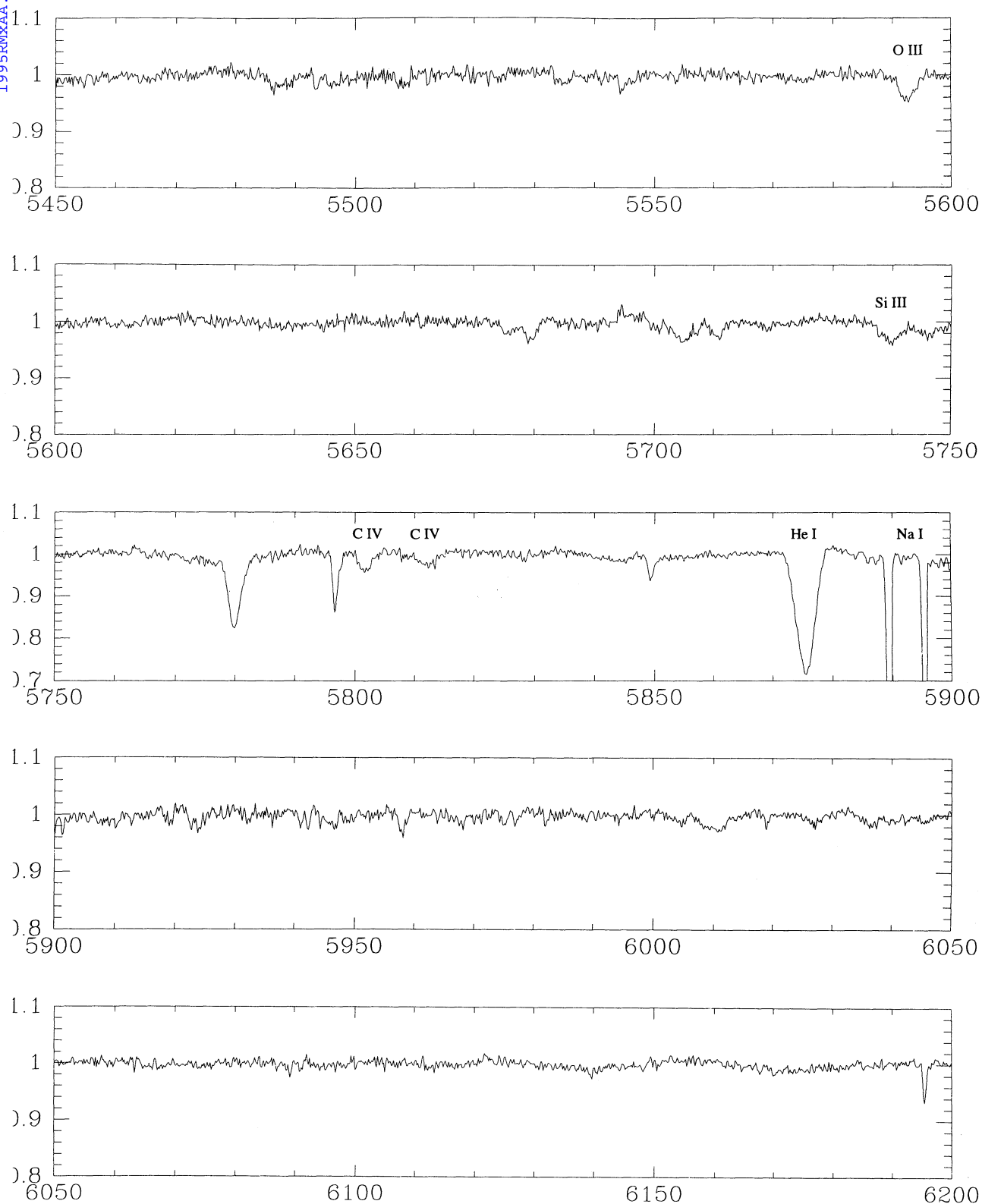CANALIZO, KOENIGSBERGER, PEÑA, & RUIZ
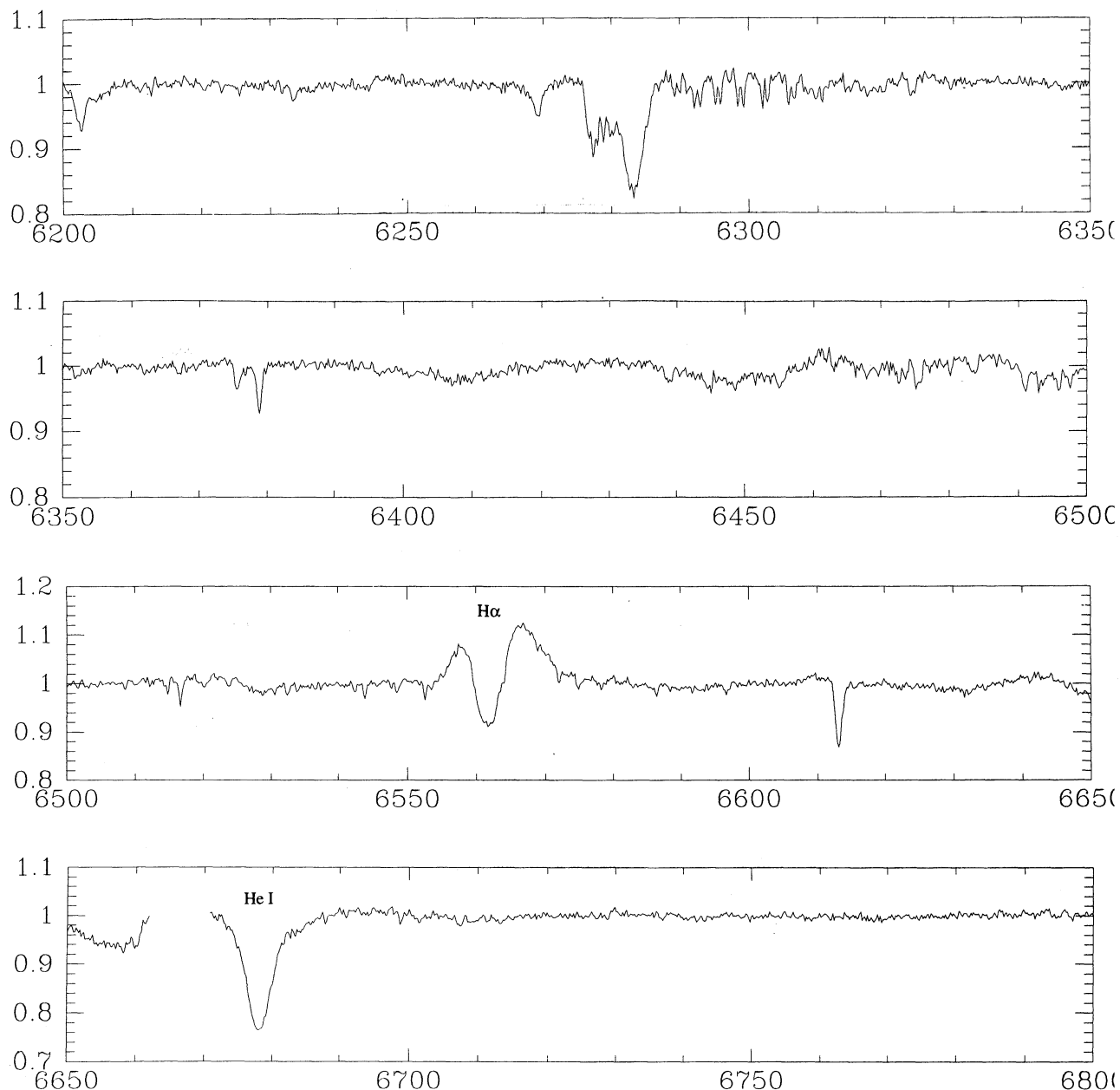
Fig. 1. Continued

Fig. 1. Continued

Fig. 1. Continued

3.2. Line Profiles

Variations in the line profiles as a function of orbital phases were detected primarily in the strong lines. In Figure 3 we illustrate the profile of He I 5876 at orbital phases 0.788, 0.335, and 0.677 on a velocity scale corrected for the orbital motion of the O supergiant. The principal variation can be described as a change in the extent of the blue wing of the line and the central position of the minimum in the absorption. There is a significant difference between the profiles at phase 0.335 and phase 0.667, both of which correspond to spectra obtained within the same orbital cycle (June 1994); profiles at all other phases, except for phase 0.149, lie within the range shown in Figure 3. There is a clear reduction in the strength of the absorption line at phase 0.677 relative to the other two phases. The velocity range most affected is from -120 to $+40$ km s^{-1} although variations out to $\simeq -240$ km s^{-1} are present. The same effect is observed at Hβ and a similar tendency is seen at other He I lines and marginally at He II 5411.

As noted in § 3.1, at phase 0.149 there is a maximum in equivalent width in some of the absorption lines, which is due to the presence of a more extended blue wing at this phase than at any other of the orbital phases for which we have data. The extended blue wing is present in the He I lines as well in Hβ; the extended blue wing is not, however, evident in Hγ or He II 5411, 4541 A. Thus, the phenomenon is associated with the lower excitation/ionization lines. It is illustrated in Figure 4, where we compare the profile of He I 5876 A at orbital phases 0.149 (broken line) and phase 0.980. At phase 0.149 the blue wing of the absorption line extends out to -260 km s^{-1} while the red wing extends only out to $\sim +160$ km s^{-1}. Such an asymmetry would be expected if the line is formed in regions of the photosphere which are already accelerating outward and form the base of the stellar wind. Furthermore, the absence of such an effect in the higher excitation/ionization lines provides further evidence in favor of this hypothesis (see below). However, why such an extended wing is present only at phase 0.149 and not at other orbital phases is not clear. It is important to note that the data for phase 0.980 and phase 0.149 were obtained during different epochs (October 1992 and June 1994, respectively) and that the variations we are reporting could be episodic, rather than periodic and orbital phase-dependent.

In Figure 5 we superpose the line profiles of Hβ, He I 5876 A and the emission line of He II 4686 A on the same velocity scale for different orbital phases. The phase-dependent profile variations we observe in He II 4686 A are qualitatively very similar to those reported by Gies & Bolton (1986b), and point to the stability in the mechanisms responsible for this variability. In Figure 5 we see that when the He II 4686 A emission line is displaced towards the blue, He I 5876 A presents a corresponding "bump" superposed on its absorption profile. A similar effect occurs when He II 4686 A is displaced towards the red. Thus, there is some evidence suggesting that contamination by variable emission components may be responsible for the profile variations shown in Figure 3.

3.3. Radial Velocity vs. Excitation Correlations

From Table 3, we have chosen the lines listed in Table 4 to measure their radial velocities at each orbital phase. These lines are, in principle, unblended, strong and/or with good signal to noise ratios, and span values of excitation potential from 20 eV to 75 eV. Lines of hydrogen were excluded because of the relatively strong line profile variations which they suffer. The radial velocities in Table 4 are corrected only for the velocity of the Earth-Sun system with no correction for the orbital motion of the O-supergiant.

In Figure 6 we present the plots of RV vs. E for 7 of the 8 orbital phases covered by our observa-

tions (phase 0.149 was excluded). We use the same definition of "excitation" as introduced by Hutchings (1976b); i.e., the excitation of a line is measured as the ionization potential of the ionization state lower than that observed plus the excitation potential of the lower level of the transition causing the line. The error bars correspond to the standard deviation about the mean (listed in Table 4). The slope of the relation was calculated by using a least squares linear fit to the data with uniform weights to each data point. Slopes were also calculated assigning weights inversely proportional to the standard deviation about the mean for each point. Note that in this paper we use the standard convention for the slope of a linear relation, while Hutchings (1976b) gives the inverse of this value divided by a constant. Our results for HDE 226868 are listed in Table 5, where the variation in the slope as a function of orbital phase is evident. The range in values we obtain is from 0.13 ± 0.05 to 0.30 ± 0.04 km s^{-1} eV^{-1} (uniform weights) and from 0.16 ± 0.06 to 0.26 ± 0.05 km s^{-1} eV^{-1} (weighted). These are consistant with the value of 0.13 km s^{-1} eV^{-1} found by Hutchings (1976b) and 0.23 km s^{-1} eV^{-1} found by Aab (1983a).

In Figure 7 we illustrate the dependence on orbital phase of the slope of the RV vs. E relations of Figure 3 (the uniform weight fits), where an abrupt increase in the slope occurs at phase 0.5. A second, less pronounced increase in slope is present near phase 0.0. This is the same type of variation that Friend & Castor (1982) predicted theoretically for the mass loss rate, as a function of the angular position on the supergiant's surface. With Θ defined as the angle from the axis of the binary system, their model for the case of the primary nearly filling its Roche lobe (Figure 4 of Friend & Castor 1982) predicts a maximum mass loss rate of $\sim 0.64 \times 10^{-6}$ $M_\odot$ yr^{-1} sr^{-1} at $\Theta = 0°$ (orbital phase = 0.5), which is a factor of four larger than the predicted mass loss rate of $\sim 0.15 \times 10^{-6}$ $M_\odot$ yr^{-1} sr^{-1} at $\Theta = 32°$ (orbital phase ~ 0.6). A second but broader maximum in the mass loss rate, with a value of $\sim 0.22 \times 10^{-6}$ $M_\odot$ yr^{-1} sr^{-1} occurs at $\Theta = 180°$ (orbital phase = 0.0). If we assume that the absolute value of the slope of the RV vs. E relation is directly proportional to mass loss rate, we can compare the ratio of predicted mass loss with the slope we derive from the present data. The ratio of these two values gives (fortuitously!) near unity at all orbital phases except at phase 0.5, where this ratio is larger than 2. It is important to note, however, that the orbital inclination of Cyg X-1 is estimated to be $i \sim 30°$ and thus the velocity we have measured at phase 0.51 is not the actual expansion velocity in the direction of the companion. If we assume that most of the contribution to the line profiles at phase 0.5 arises in that portion of the O-star photosphere expanding towards the companion,

then the true expansion velocity towards the companion is obtained by dividing our measured values by $\cos(90° - i)$. When this is done, and using $i = 30°$, we find that the slope of the RV vs. E correlation at phase 0.51 is a factor of 4 larger than at other phases (except phase 0.98), which is in excellent agreement with the predictions of mass loss rate according the Friend & Castor (1982) model.

The excellent agreement between the predicted mass loss rates and the RV vs. E slope would seem to indicate that the X-rays emitted by the collapsed companion do not significantly alter the properties of the primary star's photosphere where absorption lines of higher excitation are formed. This is not the case for the lower excitation lines where the line profile variations observed indicate that interaction effects contribute to their profiles. It is important to note that the X-ray luminosity of Cyg X-1 implies a factor of 2 smaller mass loss rates than predicted by Friend & Castor (1982). As suggested by them, this is probably a result of the conditions under which accretion is occurring. Recent calculations of the morphology of the flow in the vecinity of a collapsed companion show that the accretion process is very complicated, involving unstable bow shock and accretion disks (Livio, Soker, & Matsuda 1991; Matsuda, Inoue, & Sawada (1987), and depends strongly on the degree to which the impinging stellar wind is heated and ionized by the X-rays (Blondin et al. 1990; Blondin 1995). An interesting consequence of a modified gravitational potential model such as that of Friend & Castor (1982) is that there is enhanced mass-loss in the plane of the orbit. Although this enhancement occurs only at two points (i.e., facing and opposite to the collapsed companion), the net effect will be the presence of more ejected material in the orbital plane than perpendicular to it.

3.4. Classical Curve of Growth Analysis

We have followed the method described by Gray (1992) to perform a classical, one-layer curve of growth analysis of the spectrum of Cyg X-1. Clearly, this method has limitations for early-type stars, where the analysis of the spectra requires detailed non-LTE model atmospheres and subsequent non-LTE line formation calculations (Auer & Mihalas 1972, 1973; Kudritzki 1976). In particular, it has been shown that the line strengths of H and He lines calculated with models which assume LTE are weaker than non-LTE line strengths, the latter being in better agreement with the observations (Auer & Mihalas 1972, 1973). Thus, a curve of growth analysis which relies on LTE assumptions will yield overabundances for those ionic species which requiere non-LTE. An additional limitation to the use of the curve of growth analysis in OB stars is the limited number of lines available, especially in the optical wavelength region.

Despite the above limitations, we consider it fruitful to apply a classical curve of growth analysis to our HDE 226868 spectra since only recently have the non-LTE methods been applied to the calculation of line profiles of elements other than H and He, due to the complex problem of dealing with multi-level, non-LTE radiative transfer (see Kudritzki & Hummer 1990 for a review). Furthermore, by comparing the results of a classical analysis of two stars of similar spectral classification, differences in their relative abundances can be detected, and thus useful information can be derived.

The empirical curves-of-growth (ECG) were constructed by plotting $\log(W_\lambda/\lambda)$ vs. $\log(gf_\lambda/\lambda_r) - \Theta_{exc}\chi$ where λ_r is an arbitrary reference wavelength here chosen to be 5000 A and χ is the ionization potential. All parameters are as in Gray (1992). The gf factors were obtained from Wiese, Smith, & Glennon (1966) and Wiese, Smith, & Miles (1969).

A total of 28 absorption lines of 9 different ions between 3700 A and 6578 A were selected for the construction of the ECG. The lines selected, which are indicated by an asterisk in Table 3, have in principle, little contamination by other ionic species. In Figure 8 four of the plots of the data (He I, N III, O II, Si III) are illustrated.

We used the theoretical curve-of-growth (TCG) for the Milne-Eddington approximation given by Wrubel (1949), assuming that lines are formed by pure absorption. From these, we chose the one with $B(0)/B(1) = 10/3$ based on the average central depth of our lines, and $\log(a) = -3$, where $a = A_{ji}\lambda/4\,\pi\xi_0$ (Mihalas 1978), and assuming an effective temperature of 30000 K. Here, ξ_0 is the most probable speed of the atom. The values of A_{ji} were taken from Wiese et al. (1966). Although the calculated values of $\log(a)$ for different lines had a small scatter, -3 is a good approximation since none of our data points lie beyond the flat part of the TCG, except for He II.

The TCG ordinate is given by $\log(W_\lambda c/\lambda\xi_0)$. Thus, a vertical shift between the ECG and the TCG immediately yields ξ_0. This shift should be constant for every ion, if we assume all lines are formed at approximately the same mean depth within the atmosphere. We determined the vertical shift from the N III and He I ECG since they were constrained by the greatest number of points. The shift yields $\xi_0 = 15.73 \pm 0.18$ km s^{-1}.

The excitation temperature Θ_{exc} was determined from the lines of N III because they had the largest range in excitation potential. This was done by plotting the shifts of the ECG for different multiplets vs. their excitation potentials. The slope of this plot is equal to Θ_{exc} as shown in Figure 9. We find $\Theta_{exc} = 0.157 \pm 0.008$, equivalent to an excitation temperature T_{exc} (N III) = 32100 ± 1600 K.

TABLE 3

LINES PRESENT IN HDE 226868

λ_{lab}	Ion	W_λ (A)	Std. Dev. (A)	Comments
3324.573	N II	0.09	...	...
3330.40	O III	0.03	...	...
3334.87	Ne II	0.11	...	...
3340.74	O III	0.07	...	...
3341.53	?	0.20	...	...
3344.43	Ne II	0.02	...	...
3348.05	O III	0.10	...	...
3350.68	O III ⎤	0.06	...	...
3350.99	O III ⎦			
3354.550	He I	0.10	...	...
3357.90	Ne II	0.03	...	...
3360.63	Ne II	0.04	...	...
3362.38	O III	0.07	...	...
3367.36	N III	0.12	...	...
3376.66	O III ⎤			
3376.82	O III ⎥	0.11	...	...
3377.20	O II ⎦			
3382.69	O III ⎤			
3383.85	O III ⎥	0.13	...	...
3384.95	O III ⎦			
3388.46	Ne II	0.05	...	...
3392.78	Ne II	0.05	...	...
3400.375	?	0.09	...	...
3404.961	O III	0.12	...	...
3415.29	O III	0.18	...	...
3428.76	Ne II ⎤	0.04	...	...
3428.67	O III ⎦			
3444.10	OIII	0.04	...	...
3447.586	He I	0.17	...	...
3470.42	O II ⎤	0.03	...	...
3470.81	O II ⎦			
3512.512	He I	0.07	...	...
3514.58	He I	0.02	...	...
3554.52	He I	0.12	...	...
3561.979	HeI	0.06	...	...
3571.26	Ne II	0.02	...	...
3587.270	He I ⎤	0.24	...	...
3587.405	He I ⎦			
3613.643	He I	0.15	...	...
3634.232	He I ⎤	0.21	...	...
3634.369	He I ⎦			
3645.123	Si III	0.07	...	...
3651.97	He I ⎤	0.04	...	...
3652.12	He I ⎦			
3679.355	H21	0.05	...	...
3682.81	H20	0.03	...	...
3686.833	H19	0.02	...	...
3691.557	H18	0.01	...	...
3694.197	Ne II ⎤	0.09	...	...
3695.37	O III ⎦			
3697.15	H17	0.05	...	...
3703.86	H16 ⎤			
3705.005	He I ⎥	0.37	...	...
3705.148	He I ⎦			
3707.24	O III	0.05	...	
3709.64	Ne II	0.04	...	...
3711.97	H15	0.41	...	...
3714.03	O III ⎤	0.04	...	...
3715.08	O III ⎦			
3721.94	H14	0.28	...	...
3729.70	O III	...	...	...
3734.37	H13	0.81	...	...
3749.49	O II ⎤	0.76	...	...
3750.154	H12 ⎦			
3754.62	N III ⎤	0.24	...	...
3754.67	O III ⎦	...	...	...
3757.21	O III	0.08	...	
3759.87	O III	...	...	...
3762.435	Si IV ⎤	0.03	...	...
3762.63	O II ⎦			
3768.81	He I ⎤	1.11	...	...
3770.63	H11 ⎦			
3774.00	O III	...	...	...
3777.16	Ne II ⎤			
3777.60	O II ⎦			
3791.26	O III ⎤	0.06	...	...
3791.41	Si III ⎦			
3797.90	H10	0.69	...	...
3803.14	O II	...	...	...
3806.56	Si III	0.05	...	...
3819.61	He I ⎤	0.51	...	...
3819.76	He I ⎦			
3833.57	IIe I	...	...	...
3835.39	H9	1.04	...	...
3838.09	He I ⎤	0.07	...	...
3838.32	S III ⎦			
3842.18	N II ⎤	0.04	...	...
3842.46	Si III ⎦			
3856.16	O II	0.04	...	...
3867.48	He I ⎤	0.09	...	...
3867.63	He I ⎦			
3871.82	He I	0.08	...	*
3882.20	O II	0.03	...	...
3888.64	He I ⎤	1.11	...	...
3889.05	H8 ⎦			
3893.53	O II	...	...	...
3896.30	O II	...	...	...
3926.53	He I	0.04	...	...
3933.66	Ca II	0.39	...	interstellar
3953.08	Si III ⎤	0.05	...	...
3954.37	O II ⎦			
3961.59	O III	0.05	...	...

TABLE 3 (CONTINUED)

λ_{lab}	Ion	W_λ (A)	Std. Dev. (A)	Comments	λ_{lab}	Ion	W_λ (A)	Std. Dev. (A)	Comments
3964.73	He I	...	...	...	4317.14	O II	0.11	0.01	...
3968.47	Ca II	...	...	interstellar	4319.63	O II			
3968.34	He II	1.54	...	...	4336.87	O II			
3970.07	Hε				4338.67	He II			
3982.72	O II	0.02	...	*	4340.47	Hγ			
3995.00	N II	0.02	...	...	4345.56	O II	1.55	0.06	...
3998.69	N III	0.08	0.01	*	4347.43	O II			
4003.64	N III	0.11	0.01	*	4348.36	N III			
4009.27	He I	0.26	0.01	*	4349.43	O II			
4026.19	He I	0.76	...	...	4351.	O II	...	...	...
4026.36	He I				4366.90	O II	0.06	0.01	...
4035.08	N II	0.06	0.01	...	4379.09	N III	0.14	0.02	...
4035.09	O II				4387.9242	He I	0.39	0.02	*
4037.97	N II	0.05	0.01	...	4391.94	Ne II	0.04	0.01	...
4038.06	Si IV				4414.91	O II			
4041.31	N II	0.08	0.01	...	4416.98	O II	1.28	0.08	...
4044.54	N II	0.03	0.02	...	4428.	DIB			
4044.75	N II				4437.55	He I			
4069.634	O II				4447.03	N II	0.06	0.01	...
4069.897	O II	0.39	0.03	...	4471.479	He I	0.88	0.02	...
4070.261	C III				4471.69	He I			
4075.87	O II	0.17	0.03	...	4477.88	O II			
4078.86	O II	0.05	0.01	...	4481.13	Mg II	0.12	0.02	...
4088.86	Si IV	0.64	0.03	...	4481.33	Mg II			
4089.30	O II				4485.4	?	−0.06	0.01	emission
4097.26	O II				4501.7	DIB	0.09	0.03	...
4097.31	N III				4510.92	N III	0.12	0.01	*
4101.07	Hδ	...	...	...	4514.89	N III	0.18	0.02	
4111.26	Si III	0.04	0.01	...	4518.18	N III	0.03	0.01	...
4111.51	Si III				4523.60	N III	0.08	0.01	
4116.10	Si IV	0.46	0.02	...	4527.86	N III	0.07	0.01	...
4120.81	He I	0.24	0.03	...	4529.7	O III			
4120.99	IIe I				4534.57	N III	0.07	0.01	*
4132.81	O II	0.03	0.00	...	4541.59	He II	0.16	0.01	*
4143.76	He I	0.29	0.01		4552.62	Si III	0.17	0.02	*
4153.30	O II	0.05	0.01	...	4567.83	Si III	0.13	0.01	*
4168.97	He I				4574.76	Si III	0.10	0.03	*
4169.23	O II	0.06	0.01	...	4590.971	O II	0.08	0.00	*
4169.38	N II				4596.17	O II	0.06	0.01	...
4186.90	C III	0.09	0.01	*	4629.98	C II			
4189.79	O II	0.10	0.03	*	4630.54	N II	0.09	0.02	...
4195.70	N III	0.08	0.02	*	4631.24	Si IV			
4199.83	IIe II	0.13	0.01	...	4634.16	N III	0.16	0.03	...
4232.15	?	0.07	0.01	...	4640.64	N III			
4253.59	S III				4641.81	O II	0.29	0.05	...
4253.74	O II	0.10	0.01	...	4641.90	N III			
4253.98	O II				4647.42	C III			
4276.71	O II	0.07	0.02	*	4649.14	O II	1.14	0.03	...
4282.96	O II				4649.85	O II			
4283.70	S III	0.07	0.01	...	4654.32	Si IV			
4285.70	O II				4661.64	O II	0.07	0.01	*
4300	?	0.04	0.01	...	4665.86	C III	0.05	0.01	*

TABLE 3 (CONTINUED)

λ_{lab}	Ion	W_λ (A)	Std. Dev. (A)	Comments	λ_{lab}	Ion	W_λ (A)	Std. Dev. (A)	Comments
4673.75	O II	0.03	0.01	...	5705.12	DIB	0.13	0.01	...
4685.68	He II	...	...	emission	5710.766	N II(?)	0.06	0.01	not phot.
4699.21	O II	0.03	0.01	...	5739.73	Si III	0.07	0.01	...
4713.1455	He I	0.28	0.02	*	5746.81	Ca I(?)	0.05	0.02	...
4713.376	He I				5780.3839	Si I	0.57	0.01	interstellar
4726.4	DIB	0.23	0.03	...	5797.8591	Si I	0.16	0.01	interstellar
4727.41	C II				5801.33	C IV	0.08	0.01	...
4730.519	Si III	0.03	0.01	...	5812.14	C IV	0.06	0.01	...
4762.7	DIB	0.09	0.01	...	5849.65	DIB	0.07	0.01	...
4779.	DIB	0.05	0.02	...	5875.621	He I	1.15	0.06	...
4819.74	Si III	0.03	0.01	...	5875.966	He I			
4828.968	Si III	0.03	0.01	...	5889.9504	Na I	0.66	0.00	interstellar
4859.32	He II	1.21	0.03	...	5895.9236	Na I	0.71	0.01	interstellar
4861.332	Hβ				5926.366	Mg II	0.06	0.00	interstellar
4882.	DIB	0.10	0.02	...	6010.1	DIB	0.11	0.01	...
4921.9310	He I	0.56	0.03	*	6031.7	?	−0.03	0.01	emission
5015.6779	He I	0.43	0.01	*	6036.56	Fe III	0.04	0.01	...
5046.51	N II				6037.96	C II			
5047.11	C II	0.21	0.01	...	6113.16	DIB	0.03	0.00	...
5047.74	He I				6203.06	DIB	0.17	0.01	...
5219.37	Si II	0.06	0.02	...	6269.73	DIB	0.09	0.00	...
5235.66	?	0.03	0.00	...	6279.35	Si I	0.96	0.04	interstellar
5411.52	He II	0.29	0.01	*	6283.86	DIB			
5418.6	?	0.03	0.00	interstellar	6376.12	DIB			
5450.3	DIB	0.16	0.01	...	6377.84	C II	0.12	0.02	...
5487.53	DIB	0.13	0.01	...	6533.	DIB	...	...	...
5494.0.6	DIB	0.03	0.00	...	6562.82	Hα	0.12	0.01	emission
5508.11	O III	0.04	0.01	...	6578.05	C II	0.03	0.01	...
5592.37	O III	0.17	0.02	*	6613.62	N II	0.16	0.01	...
5676.019	N II	0.13	0.02	...	6678.15	He I	1.24	0.06	...
5679.562	N II				6741.8	DIB	0.03	0.01	...
5695.92	C III	−0.06	0.01	emission					

A similar procedure applied to O II (which, however has fewer lines and higher noise) gives a temperature consistent with that found from the N III lines, T_{exc} (O II) = 32900 ± 2800. Using T_{exc} to calculate $\xi_{thermal}$, and using the previously determined value of ξ_0, we estimate a microturbulent velocity ξ_{turb} = 10.7 km s^{-1}.

The difference between the theoretical and the empirical abscissae is equal to $\log(C)$, where C is proportional to the number of absorbers of a given ion divided by the partition function of that ion and the continuum opacity at a reference wavelength, k_c. Using a constant vertical shift, we found the horizontal shift for each of the 9 ECG. Partition functions were taken from Aller, Elste, & Jugaku (1957) for O, C, N, and Si, and from Elste & Jugaku (1957) for He.

The abundances $\log(N_{ion}/k_c)$ which were obtained are listed in column 2 of Table 6 for each of the ions listed in column 1. In column 4 of this table, we list the relative abundances taken with respect to the abundance of O III (i.e., $\log(N_{ion}/N_{O\ III})$ + $const$ where the constant was chosen to be 8.8, as in Lamers [1972b]).

The entire procedure was repeated and applied to data of ε Ori (B0Ia) taken from Lamers (1972a), chosing the same lines we used in the present analysis of HD 226868. The resulting abundance values are listed in columns 3 and 5 of Table 6. Comparing columns 4 (HDE 226868) and 5 (ε Ori), we find an excess helium abundance and an underabundance in carbon in HD 226868 with respect to ε Ori. This difference is listed in column 6.
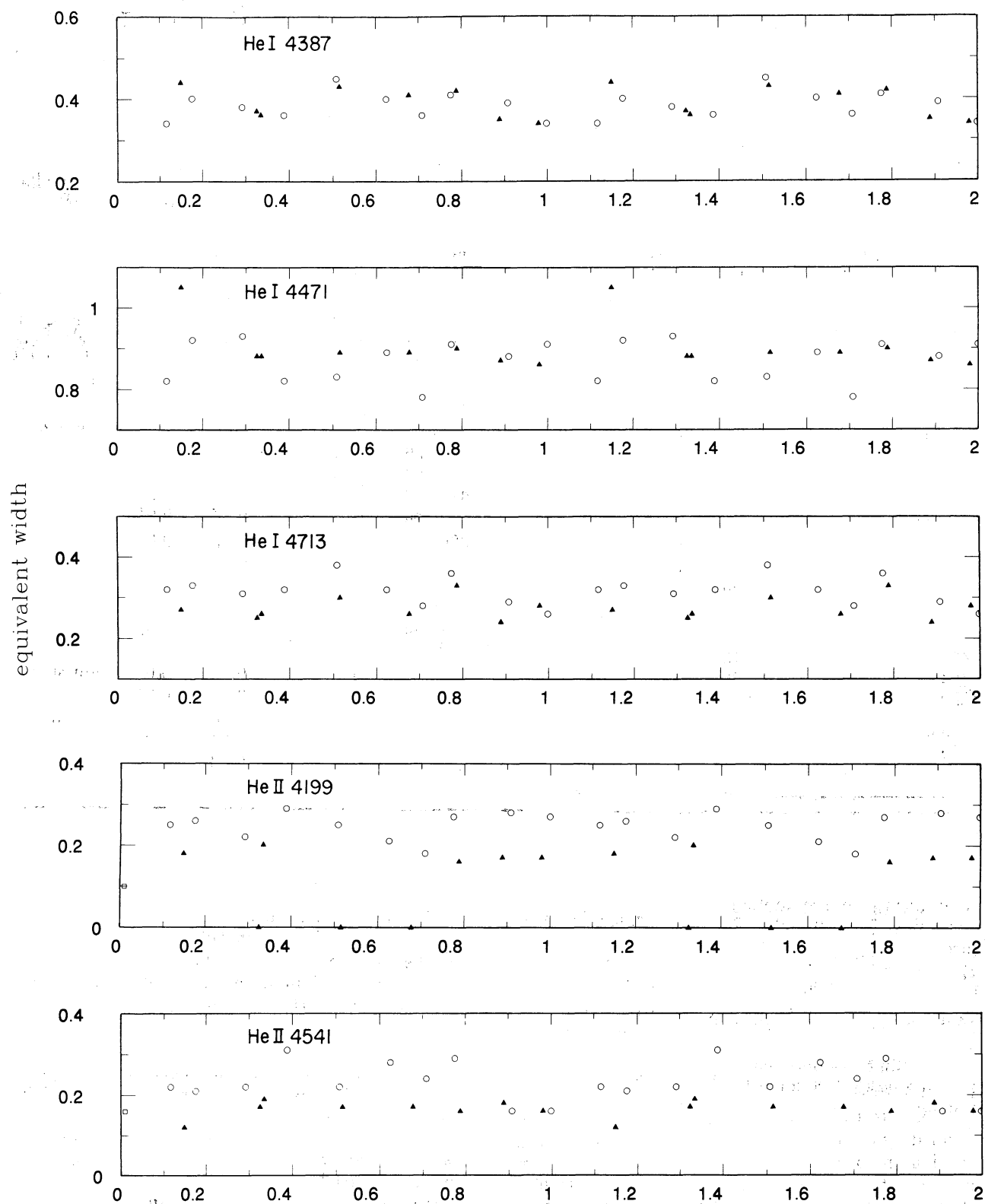
CANALIZO, KOENIGSBERGER, PEÑA, & RUIZ

Fig. 2. Equivalent widths of He I, He II, Si III and Hβ as a function of orbital phase. Circles: data of Gies & Bolton (1986a); triangles: data presented here. The uncertainty in the measurements is 5%.
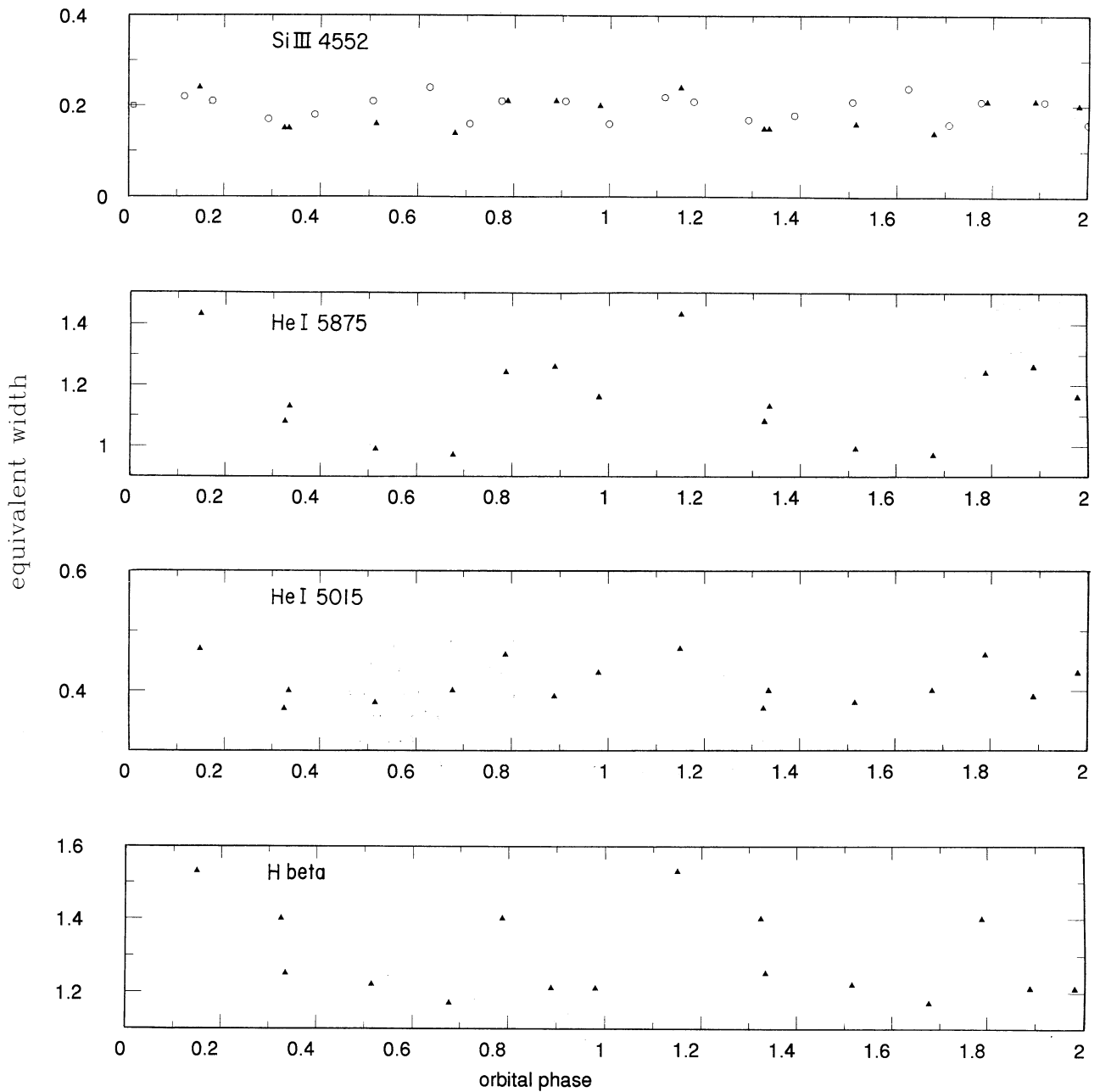
Fig. 2 Continued

4. CONCLUSIONS

We have presented the results of echelle observations of HDE 226868 in the wavelength range 3200–6800 A with the following conclusions:

1. The profiles of the emission lines and of the strong absorption lines are found to vary. The changes in He II 4686 A are qualitatively very similar to those reported previously (Gies & Bolton 1986a; Ninkov, Walker, & Yang 1987) and indicate that the mechanism responsible for the variations is very stable. The variations observed in the photospheric absorption lines affect primarily the blue wings of these lines. The lines most affected are the strongest ones, and particularly He I 5876 A and Hβ. The profile variations lead to variations as large as 25% in the values of the equivalent widths. The He II lines do not display significant variability in our data. A comparison of Hβ and He I 5876 A absorption line profiles with the emission lines of He II 4686 A and

Hα suggests that the variations in the photospheric line profiles most likely result from contamination by variable emission components.

2. RV vs. E relations are constructed for 7 orbital phases. The slope of these relations, A, varies with orbital phase, having a maximum absolute value at phase 0.5, which corresponds to the conjunction in which the collapsed object is "in front" of t he OB supergiant. A second, less pronounced maximum occurs near phase 0.0. Assuming that A is directly proportional to mass loss rate, and assuming an orbital inclination $i = 30°$ for the binary system, this result is in excellent agreement with the prediction of Friend & Castor (1982) that the modified gravitational potential due to the presence of the collapsed companion will produce anisotropic mass loss, with maximum mass-loss rates in the direction of the companion and opposite to it. The agreement between our values of A and the predicted dM/dt is best for the case in which the primary is nearly filling its Roche lobe. This "focused" stellar wind model was also shown to be consistent with the observed He II 4686 A emission line profile variations by Gies & Bolton (1986b). It is important to note that the modified gravitational potential employed by Friend & Castor (1982) assumes that the companion has 13 $M_\odot$ and thus these results support the presence of such a massive companion.

3. A classical curve-of-growth analysis yields $T_{exc} = 32100 \pm 1600°$ K for HDE 226868 and a comparison with ε Ori indicates that HDE 226868 is overabundant in He and underabundant in C, with respect to ε Ori. Given the limitations on the use of classical curve of growth (i.e., using LTE) analyses for supergiant stars, this result is preliminary. It is interesting to note, however, that non-LTE analyses of a number of supergiant stars in the Galaxy, the LMC and the SMC have disclosed overabundances of He and N. Kudritzki et al. (1987) and Schon-berner et al. (1989) have found galactic OBN stars to be He and N enriched, C strongly depleted and O unchanged with respect to solar values, indicating that we are looking at CNO processed material at the surface of the star (Maeder 1990). Our results for HDE 226868 suggest that it may have even more CNO processed material at its surface and thus is more evolved than ε Ori .

4. A large number of diffuse interstellar bands (DIBs) are present in the spectrum. An analysis of their equivalent widths in relation with other ISM features as well as with extinction in the direction of IIDE 226868 is recommended.

We arrived at an scenario for IIDE 226868 = Cyg X-1, consistent with previous investigations, of a binary system in which the primary star nearly fills its Roche lobe and whose surface is distorted by the gravitational potential of a massive collapsed companion. There is anisotropy in the mass-loss rate, as a function of angle on the surface of the primary star, leading to enhanced mass loss in the direction of the companion and opposite to it, with respect to other directions. The accretion rate onto the col-
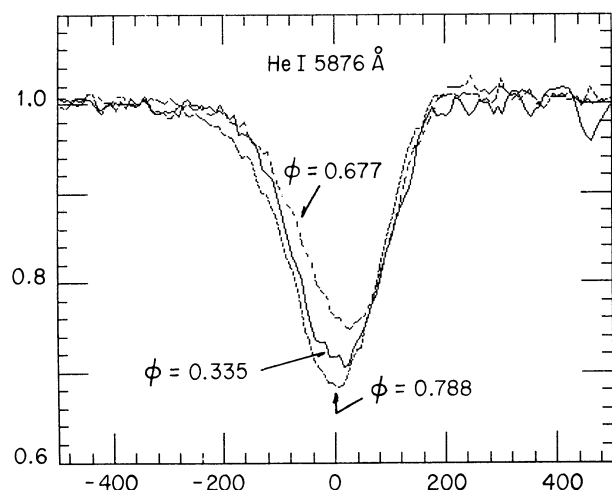

Fig. 3. Comparison of the line profiles of He I 5876 A at different orbital phases 0.788 (lowest), 0.335 (middle), and 0.677 (weakest). The abscissa is in units of velocity (km s^{-1}) corrected for the orbital motion of the O supergiant. The ordinate scale is flux normalized to the continuum level.
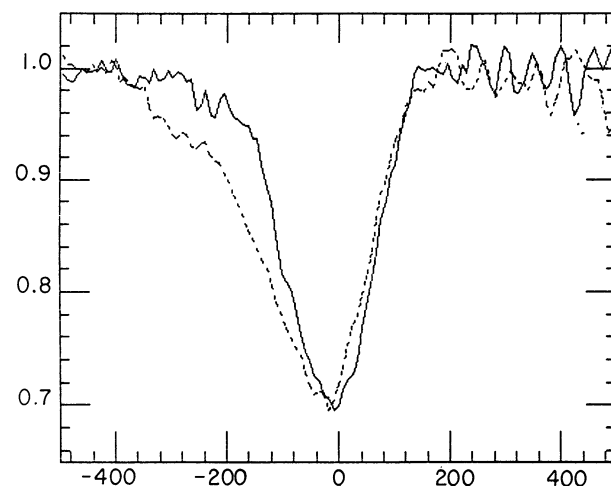

Fig. 4. Comparison of the line profiles of He I 5876 A at orbital phases 0.149 (broken line) and 0.98 (continuous line). Axes as in Fig. 3.
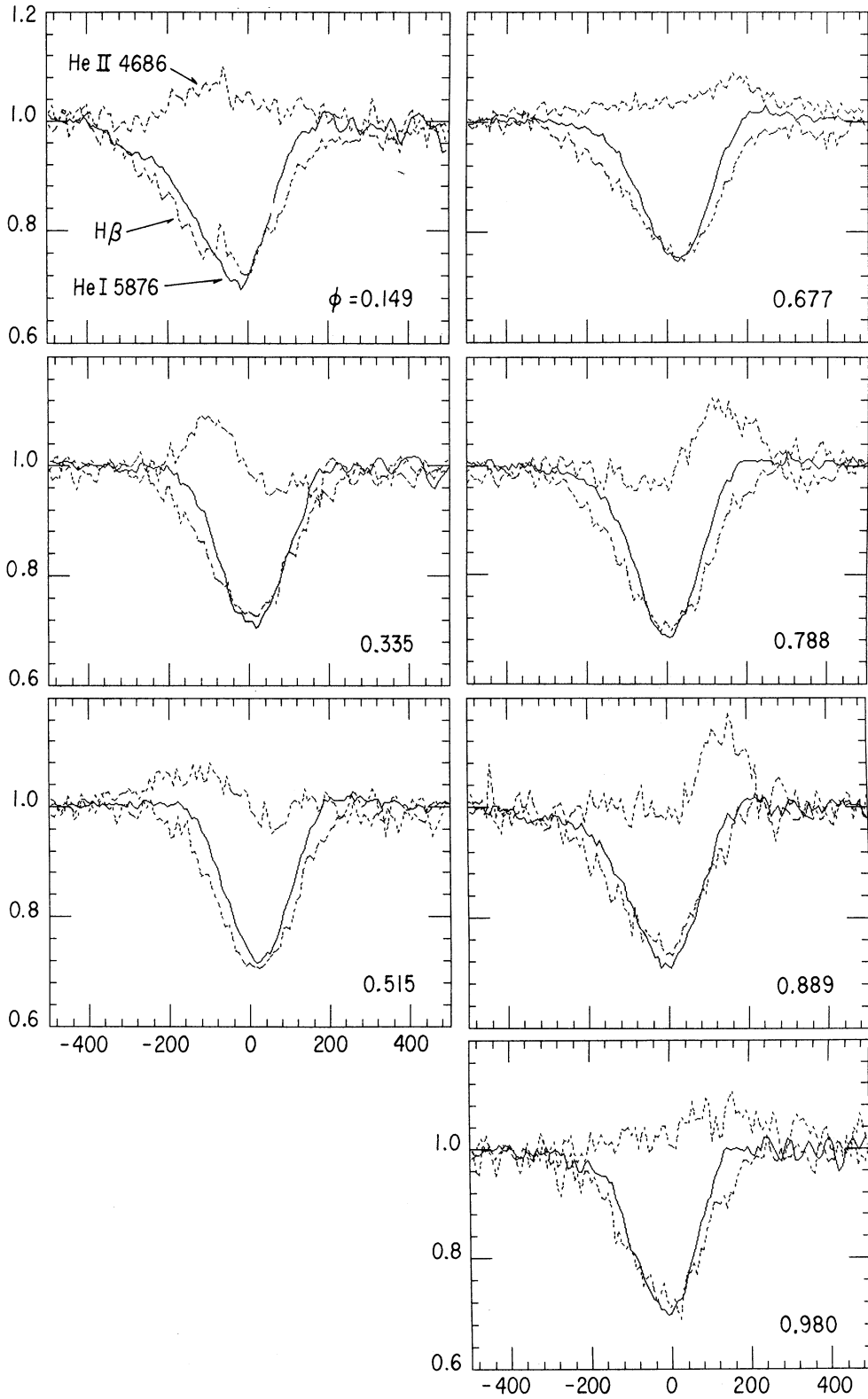
Fig. 5. Comparison of Hβ (broken line), He I 5876 A (continuous line) and the He II 4686 A emission line profiles. Axes as in Fig. 3.

TABLE 4

RADIAL VELOCITY AT DIFFERENT PHASES[a]

λ (A)	EP (eV)	Radial Velocity (Km s^{-1})						
		0.325	0.335	0.515	0.677	0.788	0.889	0.980
He I 4387.93	21.2	74	80	21	−42	−65	−48	−12
He I 4471.48	20.9	82	79	23	−46	−68	−51	−6
He I 4713.14	20.9	92	91	26	−37	−68	−43	−3
He I 4921.93	21.2	86	87	25	−41	−65	−46	−20
He I 5015.67	20.6	83	82	27	−38	−65	−46	−9
He I 5875.62	20.9	75	80	19	−44	−66	−46	−15
mean	20.9	82	83	24	−41	−66	−47	−11
std.dev	...	6	4	3	3	1	2	6
Si III 4552.62	35.3	79	82	26	−38	−65	−42	−1
Si III 4567.82	35.3	81	85	24	−41	−62	−48	−9
Si III 4574.76	35.3	86	78	27	−43	−63	−46	−12
mean	35.3	82	82	26	−41	−64	−46	−7
std.dev	...	3	3	1	2	1	3	−5
N III 4379.09	69.3	81	85	35	−34	−64	−45	−2
N III 4510.92	65.2	89	92	32	−43	−59	−36	−10
N III 4514.89	65.2	90	89	35	−42	−52	−40	7
mean	66.6	87	89	34	−40	−59	−40	−1
std.dev	...	5	3	1	5	6	4	9
O III 5592.37	69.0	88	86	38	−35	−59	−41	−1
He II 4199.83	75.6	...	85	...	...	−55	−42	8
He II 4541.59	75.6	88	92	36	−32	−59	−36	2
He II 5411.52	75.6	91	97	45	−34	−56	−36	−6
mean	75.6	90	91	40	−33	−57	−38	1
std.dev	...	2	6	6	1	2	3	7

[a] The observations at phase 0.325 have better S/N than those at phase 0.335.

TABLE 5

RADIAL VELOCITY vs. EXCITATION POTENTIAL SLOPES

phase	slope[a] uniform weights	σ	slope[a] weighted	σ
0.325	0.147	0.022	0.176	0.083
0.335	0.144	0.049	0.151	0.098
0.515	0.303	0.039	0.262	0.053
0.677	0.126	0.052	0.165	0.053
0.788	0.160	0.007	0.167	0.047
0.889	0.156	0.020	0.163	0.067
0.980	0.214	0.014	0.210	0.133

[a] km s^{-1} eV^{-1}.

TABLE 6

DERIVED ABUNDANCES

Ion	$\log(N_{ion}/k_c)$		$(\log(N_{ion}/N_{OIII})+c)$		
	Cyg X-1	ε Ori	Cyg X-1	ε Ori	diff.[a]
He I	17.94	18.53	7.53	5.93	1.60
He II	22.90	23.90	12.49	11.30	1.19
C II	14.52	16.16	4.11	3.55	0.56
C III	18.18	20.22	7.77	7.62	0.15
C IV	18.59	21.06	8.18	8.45	−0.27
N III	19.05	20.81	8.64	8.20	0.44
O II	16.84	18.76	6.43	6.15	0.28
O III	19.21	21.41	8.80	8.80	0.00
Si III	15.76	17.09	5.35	4.48	0.87

[a] Difference between Cyg X-1 and ε Ori.

Fig. 7. Slope of the radial velocity vs. excitation potential relations of Fig. 2 plotted as a function of orbital phase. Error bars correspond to the uncertainty in the fit.
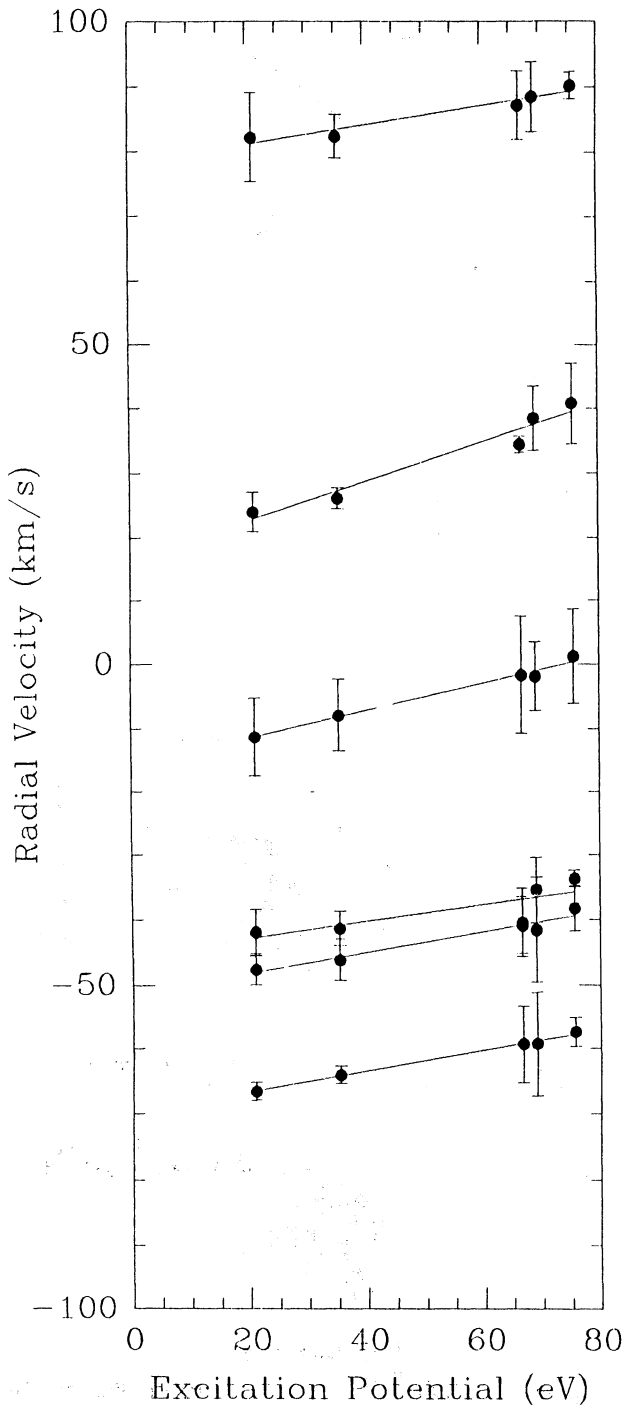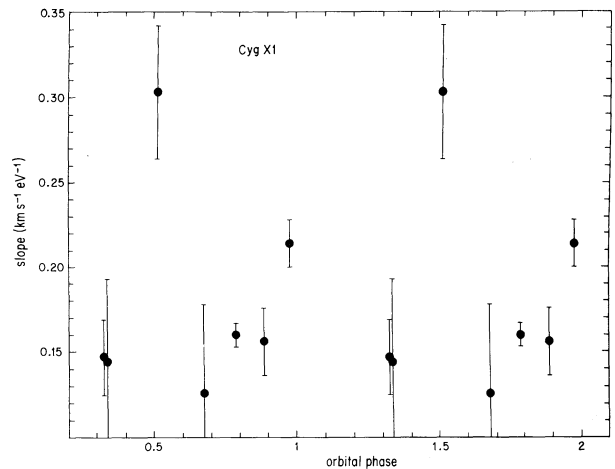

Fig. 6. Radial velocity vs. excitation potential relations for different orbital phases. Radial velocities are corrected for the Sun+Earth motion only. The excitation potential is defined as in Hutchings (1976b) and is given in eV. Error bars correspond to the standard deviation about the mean of the measures of the lines. The least-mean-squares fit was performed assuming equal weights for all points. From top to bottom the orbital phases are: 0.325, 0.515, 0.980, 0.677, 0.889, 0.788.

lapsed companion, however, is smaller than predicted by simple accretion theory due to X-ray heating of the approaching stellar wind and the complex processes involved. The only caveat to this scenario is that it relies on the hypothesis that the slope of the RV vs. E relation is proportional to mass-loss rate only. This is an issue which must be addressed in the future. Of particular interest is to model in detail the He II 4686 A and Hα emission line profiles under the assumption of the non-spherically symmetric mass loss and derive mass-loss rates from these profiles.

From our LTE curve-of-growth analysis, the primary star appears to have larger He and smaller C abundances than ε Ori, which suggests that HDE 226868 is more evolved. However, it is now very important that non-LTE analyses be applied to the individual lines in order to derive precise chemical abundances as well as T_{eff} and log g.

One final point which deserves a comment is with regard to the enhanced stellar mass loss rate in the orbital plane. This anisotropy leads to enhanced density regions in the orbital plane which will affect the evolution of the surrounding ISM during more advanced stages in the evolution of the system. Recent modelling efforts to explain the bipolar morphology of objects such as the homunculus of η Car rely on the presence of a toroidal density configuration (Frank, Balick, & Davidson 1995). It is of great interest to establish whether the binary scenario for such a configuration is applicable.
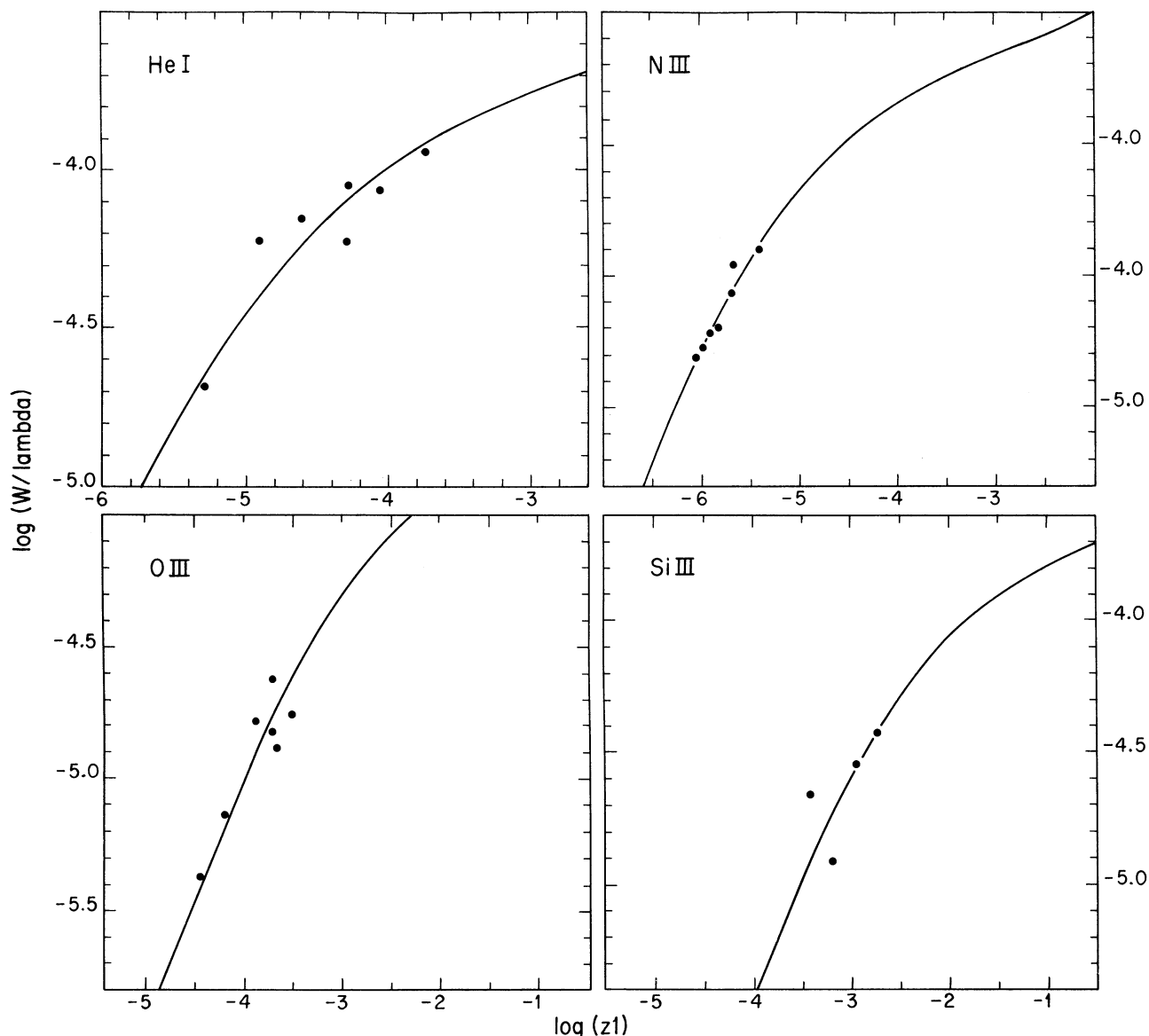
Fig. 8: Curves of growth for four of the ions included in the analysis. On the ordinate we plot $\log(W/\lambda)$ and in the abscissa $\log(gf\lambda/\lambda_r) - \Theta_{exc}\chi$. The solid line is the theoretical curve of growth given by Wrubel (1949), with $B(0)/B(1) = 10/3$ and $\log(a) = -3$.

REFERENCES

Aab, O.E. 1983a, Astrofisicheskie Issledovaniya: Izvestiya Spetsial'noi Astrofisicheskoi Observatorii, 17, 6
_____.1983b, Sov. Astron. Lett. 9, 315
Aller L.H., Elste G., & Jugaku, J. 1957, ApJS, 25, 1
Auer, L.H., & Mihalas, D. 1972, ApJ, 24, 193
_____. 1973, ApJS, 25, 433
Blondin J.M., Kallman, T.R., Fryxell, B.A., & Taam, R.E. 1990, ApJ, 356, 59
Blondin, J.M. 1995, preprint
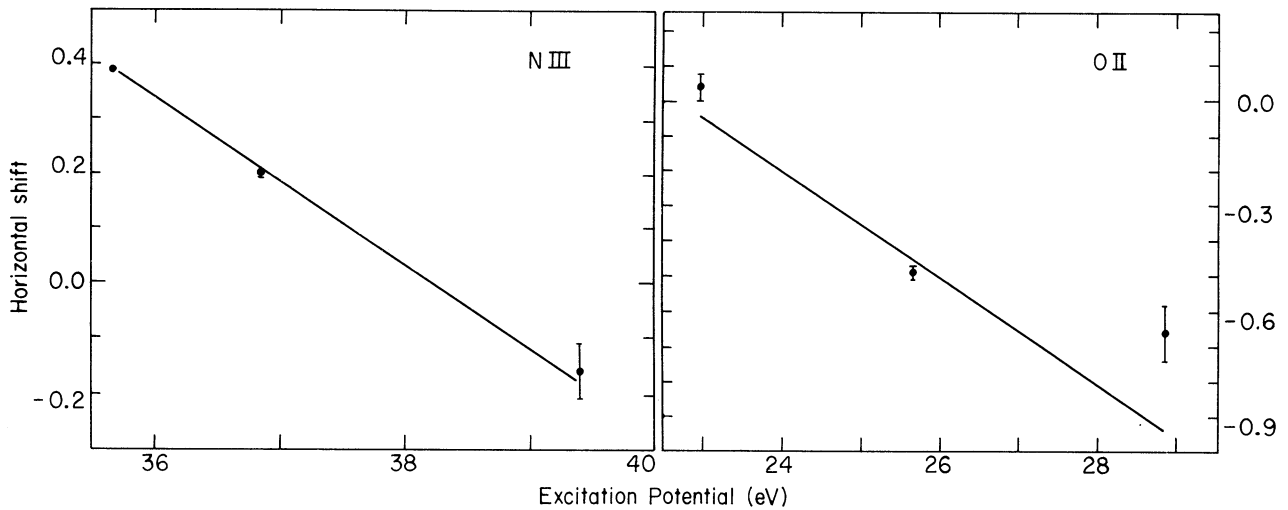Chiosi, C., & Maeder, A. 1986, ARA&A, 24, 329

Fig. 9. Excitation temperature fit using the curve-of-growth results of (a) N III and (b) O II. The best fit is achieved for N III and is $T_{exc} = 32100 \pm 1600$ K.

Cruz-González, I., & Carrasco, L. 1990, Reporte Técnico No. 61, Instituto de Astronomía, UNAM

Davis, R., & Hartmann, L. 1983, ApJ, 270, 671

Echevarría, J., & Diego, F. 1995, Publicación Técnica, Instituto de Astronomía, UNAM, in preparation

Elste, G., & Jugaku, J. 1957, ApJ, 125, 742

Frank, A., Balick, B., & Davidson, K. 1995, ApJ, 441, L77

Friend, D.B., & Castor, J.I. 1982, ApJ, 261, 293

Gies, D.R., & Bolton, C.T. 1986a, ApJ, 304, 317

———. 1986b, ApJ, 304, 389

Grey, D.F. 1992, The Observation and Analysis of Stellar Photospheres, Second Edition (Cambridge: Cambridge Univ. Press)

Hatchett, S., & McCray, R. 1977, ApJ, 211, 552

Herbig, G.H. 1995, ARA&A, 33, in press

Hutchings, J.B. 1968a, MNRAS, 141, 219

———. 1968b, MNRAS, 141, 329

———. 1976a, Publ. Dom. Ap. Obs., 14, 355

———. 1976b, ApJ, 203, 438

———. 1978, Earth and Extraterrestrial Science, 3, (Great Britain: Gordon Breach, Science Publishers), p. 123

Kemp, J.C., Barbour, M.S., Henson, G.D., Kraus, D.J., Nolt, I.G., Radostitz, J.V., Priedhorsky, W.C., Terrell, J., & Walker, E.N. 1983, ApJ, 271, L65

Kudritzki, R.P. 1976, A&A, 52, 11

Kudritzki, R.P., & Hummer, D. 1990, ARA&A, 28, 303

Kudritzki, R.P., Groth, H.G., Butler, K., Husfeld,D., Becher, S., Eber, F., & Fitzpatrick, E. 1987, in ESO Workshop on the SN1987A, ed. I.J. Danzinger (Munich: ESO Garching) p. 39

Lamers, H.J.G.L.M. 1972a, A&AS, 7, 113

———. 1972b, A&A, 17, 34

Levine, S., & Chakrabarty, D. 1994, Publicación Técnica No. MU-94-04, Instituto de Astronomía, UNAM

Livio, M., Soker, N., & Matsuda, T. 1991, MNRAS, 253, 633

Maeder, A. 1990, A&A, 84, 139

Matsuda, T., Inoue, M., & Sawada, K. 1987, MNRAS, 226, 785

Mihalas, D. 1978, Stellar Atmospheres, Second Edition (San Francisco: W.H. Freeman and Co.)

Ninkov, Z., Walker, G.A.H., & Yang, S. 1987, ApJ, 321, 438

Oda, J. 1977, Space Sci. Rev., 20, 757

Peña, D., Canalizo, G., Cardona, O., & Koenigsberger, G. 1994, Publicación Técnica, No. RT-94-07, Instituto de Astronomía, UNAM

Peña, M. & Torres-Peimbert, S. 1992, Publicación Técnica No. 97, Instituto de Astronomía, UNAM

Priedhorsky, W., Terrell, J., & Holt, S.S. 1983, ApJ, 270, 233

Shafter, A.W., Harms, R.J., Margon, B., & Katz, S.I. 1980, ApJ, 246, 612

Schonberner, D., Herrero, A., Becher, S., Eber, F., Butler, K., Kudritzki, R.P., & Simon, K.P. 1989, A&A, 197, 209

Striganov, A.R., & Svetitskii, N.S. 1968, Tables of Spectral Lines of Neutral and ionized Atoms, IFI/ Plenum, NY - Washington

Traving, G. 1957, Zeit. Ap., 41, 215

Treves, A. et al. 1980, ApJ, 242, 1114

van den Heuvel, E.P.J. 1976, in IAU Symp. 73, Structure and Evolution of Close Binary Systems, ed. P. Eggleton, S. Mitton, & J. Whelan (Dordrecht: Reidel), p. 35

Walborn, N.R. 1973, ApJ, 179, L123

Wiese, W.L., Smith, M.W., & Glennon, B.M. 1966, Atomic Transition Probabilities Vol. I, National Bureau of Reference Data System (Washington: NSRDS-NBS)

Wiese, W.L., Smith, M.W., & Miles, B.M. 1969, Atomic Transition Probabilities Vol. II, National Bureau of Reference Data System (Washington: NSRDS-NBS)

Wrubel, M.H. 1949, ApJ, 109, 66

G. Canalizo: Institute for Astronomy, University of Hawaii, 2680 Woodlawn Drive, Honolulu, HI 96822, USA

Gloria Koenigsberger: Instituto de Astronomía, UNAM, Apartado Postal 70-264, 04510 México, D.F., México (gloria@astroscu.unam.mx).

D. Peña and Elfego Ruiz: Instituto de Astronomía, UNAM, Apartado Postal 70-264, 04510 México, D.F. México.